# **Implications of Data Topology for Deep Generative Models**

Yinzhu Jin  $^{1,*}$ , Rory McDaniel  $^1$ , N. Joseph Tatro  $^2$ , Michael J. Catanzaro  $^3$ , Abraham D. Smith  $^{3,5}$ , Paul Bendich  $^{3,4}$ , Matthew B. Dwyer  $^1$ , and P. Thomas Fletcher  $^{1,6}$ 

Correspondence\*: Yinzhu Jin yj3cz@virginia.edu

#### ABSTRACT

- Many deep generative models, such as variational autoencoders (VAEs) and generative 3 adversarial networks (GANs), learn an immersion mapping from a standard normal distribution in a low-dimensional latent space into a higher-dimensional data space. As such, these mappings 5 are only capable of producing simple data topologies, i.e., those equivalent to an immersion of 6 Euclidean space. In this work, we demonstrate the limitations of such latent space generative 7 models when trained on data distributions with non-trivial topologies. We do this by training these models on synthetic image datasets with known topologies (spheres, torii, etc.). We then show 9 how this results in failures of both data generation as well as data interpolation. Next, we compare 10 this behavior to two classes of deep generative models that in principle allow for more complex data topologies. First, we look at chart autoencoders (CAEs), which construct a smooth data 12 13 manifold from multiple latent space chart mappings. Second, we explore score-based models, e.g., denoising diffusion probabilistic models, which estimate gradients of the data distribution 14 without resorting to an explicit mapping to a latent space. Our results show that these models 16 do demonstrate improved ability over latent space models in modeling data distributions with complex topologies, however, challenges still remain.
- 18 Keywords: deep generative models, topological data analysis

# 1 INTRODUCTION

- 19 Recent advances in deep generative models (DGMs) have resulted in the unprecedented ability of these
- 20 models to produce realistic data, including imagery, text, and audio. While qualitative evaluation of
- 21 generated data makes it clear that DGMs are improving at a rapid pace, quantifying how well a model
- 22 produces samples similar to the original data distribution on which it was trained is a challenging task
- 23 and an area of active research. Inherent to this problem is that generative models are fundamentally

<sup>&</sup>lt;sup>1</sup>Department of Computer Science, University of Virginia, Charlottesville, VA, USA

<sup>&</sup>lt;sup>2</sup>STR, Vision and Image Understanding Group, Woburn, MA, USA

<sup>&</sup>lt;sup>3</sup>Geometric Data Analytics, Inc., Durham, NC, USA

<sup>&</sup>lt;sup>4</sup>Department of Mathematics, Duke University, Durham, NC, USA

<sup>&</sup>lt;sup>5</sup> Math, Stats, and CS Dept. University of Wisconsin-Stout, Menomonie, WI, USA

<sup>&</sup>lt;sup>6</sup>Department of Electrical and Computer Engineering, University of Virginia, Charlottesville, VA, USA

meant to produce data that would be judged to be realistic to a human observer, and quantifying human perception—of images, language, or audio—is a difficult task.

A common approach to evaluating a generative model is to compute an empirical distributional distance between a sample from the data distribution and a sample generated by the model. For example, in computer vision, the Fréchet inception distance (FID) (Heusel et al., 2017) is a popular choice for such a distance metric. The FID approximates both the data distribution and the generated image distribution as multivariate normal distributions on the outputs of an Inception v3 model trained on ImageNet. The Fréchet distance between the resulting multivariate normal distributions is then computable in closed-form. More recently, precision and recall (Sajjadi et al., 2018) were proposed to separately evaluate how close generated samples are to the data distribution (precision) and how well they cover the data distribution (recall).

The manifold hypothesis of machine learning informally states that data distributions naturally lie near lower-dimensional manifolds embedded in the higher-dimensional Euclidean space formed by their raw representations. One class of DGMs, including variational autoencoders (VAEs) (Kingma and Welling, 2014) and generative adversarial networks (GANs) (Goodfellow et al., 2014), attempt to model the data manifold explicitly. They do this by generating data by mapping points from a prior distribution in a lower-dimensional latent space into the data representation space. This has led researchers to investigate the manifold properties of such DGMs and use manifold methods to evaluate their quality. Shao et al. (2018) develop algorithms for computing geodesic curves and parallel translation of VAEs. They observed that while VAEs were able to capture the curvature of synthetic data manifolds when trained on real image data, the manifolds generated by VAEs were nearly flat. Arvanitidis et al. (2018) propose that deterministic generators lead to a distortion of the data manifold in the latent space that fails to capture the intrinsic curvature of the data. They propose a stochastic Riemannian metric to correct for this and show that this results in improved variance estimates. Chen et al. (2018) demonstrate that Riemannian geodesics in the latent space of a DGM give better interpolations and visual inspection of generated data. Shukla et al. (2018) show that disentangled dimensions of the latent space of a VAE demonstrate higher curvature.

While these works have investigated the differential and metric geometry of DGMs, less is known about the topological properties of DGMs. Theoretically, models that generate data from a continuous mapping of a Gaussian prior distribution into Euclidean space, such as VAEs and GANs, are not able to faithfully reproduce data with non-trivial topology (e.g., spheres, tori, or other spaces with "holes"). In practice, these models may be able to perform fairly well in approximating non-trivial data topologies by shifting density away from holes. The chart autoencoder (CAE) model by Schonsheck et al. (2019) extends the topological abilities of VAEs/GANs by modeling a manifold topology with multiple overlapping charts. On the other hand, DDPMs and their relatives have no topological constraints in theory. However, the topological abilities of these various DGMs have not been empirically tested or compared. This paper empirically tests the ability of generative models to handle data arising from distributions with underlying topology, and is, to the best of our knowledge, the first systematic study in this direction. There have been papers that use topological techniques, such as Manifold Topology Divergence (Barannikov et al., 2021) or Geometry Score (Khrulkov and Oseledets, 2018), to quantify the quality of data produced by generative models. More broadly, there has been extensive recent work (Hensel et al., 2021) at the interface of TDA and DL/ML. These range from methods (e.g., Chen et al. (2019); Solomon et al. (2021); Nigmetov and Morozov (2022)) that integrate TDA-based loss functions into DL algorithms, to bespoke DNN architectures (Carrière et al., 2020) that incorporate layers that process persistence diagrams, to works (e.g., Naitzat et al. (2020); Wheeler et al. (2021)) that use TDA to analyze the structure of data as it moves through DNN layers.

This paper is organized as follows. In Section 2 we review the methods used in this paper, namely, the 67 DGMs and metrics for evaluating their quality, including persistent homology. In Section 3 we present 68 our experiments comparing the ability of three DGMs—VAE, CAE, and DDPM—to learn to generate 69 data with known non-trivial topologies. To do this, we use two synthetic image datasets with a torus and 70 71 sphere topology, respectively, and a real dataset of conformations of cyclooctane, which is known to have topology equivalent to a Klein bottle intersecting with a 2-sphere (Martin et al., 2010). Note that this test 72 73 is even more difficult from a topological perspective, as the cyclooctane conformations form a topology 74 that is non-manifold, but rather a more complicated stratified space (in this case, the intersection of two 75 manifolds). Finally, in Section 4 we discuss conclusions from these experiments and future directions.

# 2 BACKGROUND AND METHODS

In this section, we first review the three deep generative models (VAEs, CAEs, and DDPM) that we evaluated for their ability to learn data distributions with non-trivial topology. Next, we describe the evaluation metrics used for our study, both related and unrelated to the topological structure.

# 79 2.1 Deep Generative Models

Various structures for deep generative models have been proposed over time. Some of the popular models are normalizing flows (Rezende and Mohamed, 2015), variational autoencoders (Kingma and Welling, 2014), generative adversarial networks (Goodfellow et al., 2014), deep energy-based model (Du and Mordatch, 2019), and the recent denoising diffusion models (Ho et al., 2020). Each type of generator has different variations. Yet, topology is rarely considered in the design. Here we choose three models to discuss.

#### 2.1.1 Variational Autoencoders

86

A variational autoencoder (VAE) is a type of encoder-decoder generative model proposed by Kingma and Welling (2014). Unlike the traditional autoencoder (Hinton and Salakhutdinov, 2006), a VAE models the probability distribution of the latent representation, z, of each data point instead of a deterministic latent representation. A VAE models the marginal log-likelihood of the ith data point,  $x^{(i)}$ , as:

$$\log p_{\theta}\left(x^{(i)}\right) = D_{KL}\left(q_{\phi}\left(z \mid x^{(i)}\right) \middle\| p_{\theta}\left(z \mid x^{(i)}\right)\right) + \mathcal{L}\left(\theta, \phi; x^{(i)}\right),\tag{1}$$

where  $\theta$  is a vector of the parameters for the generative model, and  $\phi$  is a vector of the parameters for the variational approximation. The objective is to maximize the evidence lower bound (ELBO), which is derived to be:

$$\mathcal{L}\left(\theta, \phi; x^{(i)}\right) = -D_{KL}\left(q_{\phi}\left(z \mid x^{(i)}\right) \middle\| p_{\theta}(z)\right) + \mathbb{E}_{q_{\phi}}\left[\log p_{\theta}\left(x^{(i)} \mid z\right)\right],\tag{2}$$

Usually the prior  $p_{\theta}(z)$  is set to be an isotropic Gaussian,  $\mathcal{N}(\mathbf{0}, \mathbf{I})$ . The encoder also models the  $q_{\phi}(z \mid x^{(i)})$  as a Gaussian distribution  $\mathcal{N}(\mu^{(i)}, (\sigma^{(i)})^2 \mathbf{I})$ . Therefore, the first term is easy to compute with predicted mean and variance of  $q_{\phi}(z \mid x^{(i)})$ . On the other hand, the equation for the second term of the lower bound depends on what probability distribution we assume in the data space. For example, using an isotropic Gaussian distribution leads to the mean squared error loss, and using a Bernoulli distribution corresponds to minimizing the binary cross entropy loss.

As discussed above, VAEs usually assume a Gaussian distribution in the latent space. Although this might 100 be a reasonable assumption for many data with trivial topology, it might cause problems when this is not 101 the case. Even in a simple case where the data has an  $\mathbb{S}^1$  topology which is a loop, the neural network could 102 struggle to learn a mapping from two different topological spaces. Although one might argue the Gaussian 103 can be deformed enough so that it resembles a loop in practice, we still need experiments to investigate 104 this issue. Similarly, generative adversarial networks (Goodfellow et al., 2014) also use a Gaussian prior 105 distribution in the latent space, and therefore might as well have problems learning data with non-trivial 106 topology. 107

#### 108 2.1.2 Chart Autoencoders

In many applications of the VAE, its learned latent space is often treated as a linear space. For instance, 109 generating interpolations between two points of a given dataset is often performed by generating the linear 110 path between the embeddings of these points in latent space. This operation implicitly assumes that the 111 geodesics between points correspond to linear paths in latent space. Yet, we know there exist manifolds, 112 such as the sphere  $S^2$ , which are not homeomorphic to a single linear space. It follows that the latent 113 space learned by a VAE trained on such a manifold is not geometrically faithful. That is the latent space 114 either contains a point that decodes to a point off the manifold, or the space cannot capture all geodesic 115 paths. To this end, recent architectures have been introduced to rectify this problem. We consider one such 116 architecture, the chart autoencoder (CAE) (Schonsheck et al., 2019). 117

Chart autoencoders are a generative model architecture motivated by the concept of an atlas in differential 118 geometry. In comparison to the VAE, we learn a set of k encoders and decoders parameterized by  $\{\phi_i\}_{i=1}^k$ 119 and  $\{\theta_i\}_{i=1}^k$  respectively. Each corresponding encoder and decoder is affiliated with a *latent chart*,  $Z_i$ . Thus, 120 the latent space of the CAE is composed of a set of linear latent spaces. The CAE output is determined 121 122 by a chart prediction network, P. In the original work, P maps x from the input space X to  $p \in \mathbb{R}^k$ , where p represents the vector of log probabilities of the chart membership of x. In training, the output 123 of the CAE is taken to be the sum of the outputs from the k decoders weighted by the chart prediction 124 vector, p. During evaluation, the output is taken to be that of the decoder corresponding to the likeliest 125 chart via p. In this work, we update the chart prediction network to map from the direct sum of the latent 126 embeddings,  $z_i$ , instead of x. This change was made to allow generations from the latent space without 127 reference to any network input. Intuitively, this chart prediction network is analogous to the chart transition 128 129 function affiliated with a geometric atlas. Indeed, the CAE is capable of transitioning between the outputs of different latent charts when a linear interpolation is performed in latent space. 130

#### 2.1.3 Denoising Diffusion Probabilistic Models

131

In contrast to the previous two models, the denoising diffusion probabilistic model (DDPM) proposed by Ho et al. (2020) does not have a low-dimensional latent space. It is based on the diffusion probabilistic model by Sohl-Dickstein et al. (2015), which learns to reverse a diffusion process in which Gaussian noise is gradually added to the original image,  $x_0$ , for T timesteps until we get a sampled image  $x_T$  that is nearly pure noise. We call the diffusion process that adds noise the forward process, which is a Markov chain. The reverse process is also defined to be a Markov chain as follows:

$$p_{\theta}(x_{0:T}) \coloneqq p(x_T) \prod_{t=1}^{T} p_{\theta}(x_{t-1} \mid x_t), \quad p_{\theta}(x_{t-1} \mid x_t) \coloneqq \mathcal{N}(x_{t-1}; \mu_{\theta}(x_t, t), \Sigma_{\theta}(x_t, t)),$$
 (3)

- where  $\beta_t$ 's define the variance schedule and  $\theta$  is the parameter vector of the model that learns the reverse
- 139 process. During training, we can optimize the lower bound of the log-likelihood.
- In the DDPM,  $\beta_t$  is fixed and therefore the first term of the loss can be ignored.  $\Sigma_{\theta}(x_t, t)$  is also fixed
- 141 for each time step t. Then DDPM reparameterizes  $x_t$  with the added noise  $\epsilon \sim \mathcal{N}(\mathbf{0}, \mathbf{I})$ , and  $\mu_{\theta}(x_t, t)$  with
- 142  $\epsilon_{\theta}(x_t)$ , which means the model is now trained to predict the noise  $\epsilon$ . Their experiments also show that
- omitting the different weights dependent on t does not compromise the final performance, which results in
- 144 the final loss:

$$\mathcal{L}_{simple}(\theta) := \mathbb{E}_{t,x_0,\epsilon} \left[ \left\| \epsilon - \epsilon_{\theta} (\sqrt{\bar{\alpha}_t} x_0 + \sqrt{1 - \bar{\alpha}_t} \epsilon, t) \right\|^2 \right], \tag{4}$$

- 145 with  $\bar{\alpha}_t$ 's being expressions of  $\beta_t$ 's. It is also worth noting that Song et al. (2021) derived the same model
- 146 from the view of a score based model, which learns the gradient of the log probability density in the data
- 147 space.
- We can see that the DDPM does not assume any topology on the original data distribution. The sampling
- only depends on the fact that the diffused data distribution is Gaussian, which is achieved by using a prefixed
- 150 time variance schedule. Therefore, theoretically, it should be able to learn the data of any topological
- 151 structure. Yet, this needs to be examined through experiments. Similarly, energy based models (Du and
- 152 Mordatch, 2019) also do not assume any topology on the data distribution, and during sampling start from
- 153 Gaussian distribution and then travel to high probability regions of the data space. Thus, we could expect a
- 154 similar ability in learning distributions of non-trivial topology.

# 155 2.2 Quantitative Metrics for Evaluating DGMs

- Given the purpose of DGMs is to generate samples that are as realistic as possible for a human, the
- 157 straightforward evaluation method would be the judgments by human eyes. However, there have been
- 158 attempts to quantitatively measure their performances.

#### 159 2.2.1 Wasserstein Distance

- We propose to evaluate how well a generative model learns a data probability distribution using a sample
- 161 approximation to the  $L_2$  Wasserstein 2-distance. By definition this should be:

$$W_2(\mu, \nu) = \inf_{\gamma \in \Gamma(\mu, \nu)} \left( \mathbb{E}_{(x, y) \sim \gamma} \|x - y\|^2 \right)^{1/2}, \tag{5}$$

- where  $\mu$  and  $\nu$  are probability measures of the ground truth data and the generative model, respectively,
- 163  $\Gamma(\mu,\nu)$  is the set of any joint distribution of x and y such that  $\int \gamma(x,y)dy = \mu(x)$  and  $\int \gamma(x,y)dx = \nu(y)$ .
- 164 We implement the empirical version as:

$$W_2(\mu, \nu) = \inf_{\pi} \left( \frac{1}{n} \sum_{i=1}^n \|X_i - Y_{\pi(i)}\|^2 \right)^{1/2}, \tag{6}$$

- where  $X_1, X_2, ..., X_n$  are random samples from  $\mu$ , and  $Y_1, Y_2, ..., Y_n$  from  $\nu$ , and  $\pi$  is any permutation of
- 166 1, 2, ..., n. Since the datasets are simulated, we can easily sample from the ground truth data distribution  $\mu$ .
- 167 The best  $\pi$  is obtained using the Jonker–Volgenant algorithm (Jonker and Volgenant, 1988) implemented
- 168 by SciPy (Virtanen et al., 2020).
- There are some existing works, e.g., (Genevay et al., 2018), that train generative models from the
- 170 viewpoint of optimal transport, and therefore include the Wasserstein distance in the training loss. However,

- to the best of our knowledge, we are the first to employ Wasserstein distance to evaluate how well generators
- learn the overall data distribution. The high time complexity  $(O(n^3))$  of the Jonker-Volgenant algorithm
- 173 forbids us from using too large sample sizes to represent ground truth and learned distributions. Therefore,
- one concern is whether the set of samples can adequately cover the whole distribution. However, in our
- experiments, we use data from known low-dimensional distributions that can be reasonably covered with
- 176 relatively fewer samples.

# 177 2.2.2 Fréchet Inception Distance

- 178 Fréchet Inception Distance (FID) is computed by computing the Wasserstein distance on two probability
- 179 distributions obtained by feeding a set of ground truth examples and a set of fake examples to an embedding
- 180 function. The embedding function generally used is Inception v3 trained on ImageNet with the final layer
- truncated, yielding a 2048-dimensional vector for each sample. A normal distribution is fit in this space
- 182 for each of the ground truth and fake sets, which are then the direct inputs for the Wasserstein distance.
- 183 While FID has been shown to usually align with human judgement Heusel et al. (2017), it has a number
- 184 of shortcomings Chong and Forsyth (2020); Parmar et al. (2022). Despite its shortcomings, FID has
- 185 established itself as the de facto standard metric for judging the quality of generative images Borji (2022).

# 186 2.2.3 Density, Coverage

- A line of work has defined metrics that separate failure modes by using multi-valued metrics. For example,
- a metric might focus on *fidelity* which captures the degree to which a generated image resembles those in a
- 189 dataset, whereas another might focus on diversity which captures the degree to which a sample reflects the
- 190 variation in generative factors that gives rise to a dataset.
- The earliest work, Precision and Recall Sajjadi et al. (2018), introduces two metrics that successfully
- 192 separate dropping and adding modes (recall) from image quality (precision), but have some shortcomings
- 193 including not being robust to outliers and requiring more significant tuning to be accurate.
- Density and Coverage Naeem et al. (2020) address these limitations by, still in an embedding space,
- 195 defining a manifold for a set of ground truth examples and measuring how often generated points land in it.
- 196 For their reported results, they use the 4096-dimensional layer of a truncated VGG16 trained on ImageNet
- 197 as the embedding space. They then form the real manifold as k-nearest neighbor balls for each real point.
- 198 Density is then a cumulative measure of how many real neighborhood balls the generated points land in,
- 199 normalized for the number of points. Intuitively, this value is greater than 1 when many generated samples
- 200 occur in a few real modes and less than 1 when the generated samples are too diverse or don't fall in real
- 201 modes. The other half of the metric, Coverage, is then the percentage of real neighborhood balls that have
- 202 a generated point within them. Intuitively, this is 1 when all modes of the original data are covered, and
- 203 less than 1 otherwise.

# 204 2.2.4 Topological Data Analysis: Persistent Homology

- Here we give some brief intuition about the information carried by the *persistent homology* of a point
- 206 cloud. Readers interested in a fuller and more rigorous discussion are pointed to textbooks such as
- 207 Edelsbrunner and Harer (2010) or Oudot (2017).
- Suppose that  $X = \{x_1, \dots, x_n\}$  is a point cloud in some Euclidean space. For example, let X be the
- 209 collection of points on the left of Figure 1. The persistence diagram  $D_k(X)$  is a compact summary of some
- 210 of the k-dimensional multi-scale shape information carried by X. We now give some more details about
- 211 what this means.

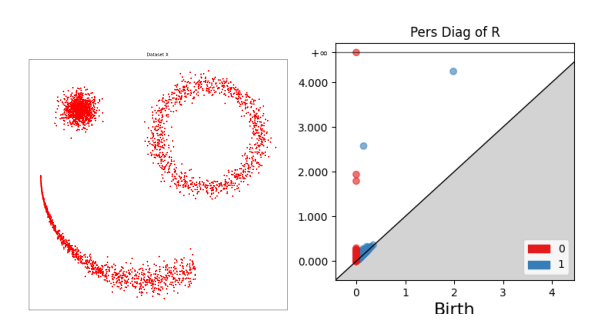


**Figure 1.** Illustration of persistence diagrams (right) for the Rips homology filtration on a point cloud (left). Persistence is shown in dimensions zero (red) and one (blue).

For each threshold value  $r \ge 0$ , let  $X_r = \bigcup_{i=1}^n B_r(x_i)$ . Note that whenever r < s, we have  $X_r \subset X_s$ , 212 and as r moves from 0 to  $\infty$ , the union of balls around the points in X grows from the points themselves to 213 the entire Euclidean space. During this process, various shape changes occur. In our working example, as r 214 increases, the number of connected components, which began as |X|, rapidly becomes 3 as clusters form 215 and then subsequently decreases as those clusters merge. The r values at which these mergers happen are 216 recorded as death values and stored in the zero-dimensional persistence diagram  $D_0(X)$ ; see the red dots 217 on the right side of Figure 1. The higher-level connectivity of the union of balls also changes as r increases. 218 In our working example, an annulus forms in the upper right of X at a very small value of r, and a ring 219 appears connecting the three clusters at a larger value of r. In technical terms, these features are called 220 one-dimensional homology classes Edelsbrunner and Harer (2010) and have rigorous algebraic definitions. 221 The r values at which they first appear are called birth value. Each homology class eventually fills in as r 222 increases; for example, the annulus at the upper right fills in at the apparent radius of the feature. These 223 death values of the one-dimensional features are paired with the birth values that created the feature, and 224 they are plotted in the one-dimensional persistence diagram  $D_1(X)$ ; see the blue dots on the right side of 225 Figure 1. 226

Thus, each persistence diagram  $D_k(X)$  consists of a (multi-)set of dots in the plane, with each dot recording the birth and death value of a k-dimensional homological feature. Intuitively 0 and 1 dimensional features represent connected components and loops/holes, respectively. Not shown in this example are two-dimensional features, which represent voids, and still higher-dimensional features. The *persistence* of a feature is the vertical distance of its dot to the major diagonal y = x in the persistence diagram. Higher-persistence features are generally thought of as genuine representatives of the underlying space, while lower-dimensional features are more likely to be caused by sampling noise. This intuition can be formalized in inference theorems (e.g. Cohen-Steiner et al. (2007), Fasy et al. (2014)).

Persistence diagrams of point clouds are computed by transforming the growing union of balls into combinatorial objects called filtered simplicial complexes. Without going into the technical details here, we note that many software packages for doing this exist (Otter et al. (2017) gives a nice overview), and that the experiments in this paper use giotto-tda (Tauzin et al., 2021).

#### 3 EXPERIMENTS

# 3.1 Datasets

227 228

229

230231

232

233

234

239

We conduct experiments on two synthetic image datasets and one real dataset. Samples of each dataset are shown in Figure 2.

255

256

257

258

259

260

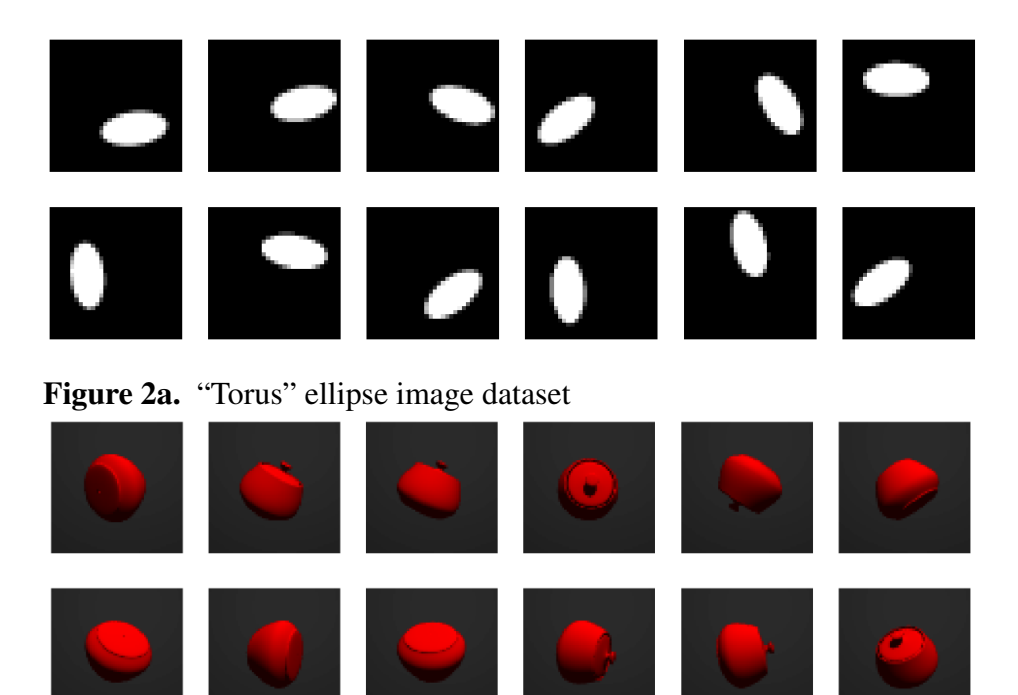


Figure 2b. Rotating jar image dataset

Figure 2. Samples from each dataset.

The "torus" ellipse image dataset contains 10,000 grayscale images of white ellipses on black backgrounds. Each image is of size  $32 \times 32$  and contains one ellipse. The images are downsampled from  $64 \times 64$  images so the edges of ellipses are blurred. The ellipse can rotate around itself 0 to  $\pi$ . And because the ellipse is 180—degree rotation symmetric, it renders the topology of  $\mathbb{S}^1$ . The center point position of the ellipse rotates 0 to  $2\pi$  around the center of the image with a radius of 7 pixels, which independently renders another  $\mathbb{S}^1$  topology. In combination this results in  $\mathbb{S}^1 \times \mathbb{S}^1$  topology, i.e. a torus topology.

The rotating jar image dataset is generated using POV-Ray by Persistence of Vision Pty. Ltd. (2004). There are 10,000 RGB colored samples of size  $64 \times 64$ . Each image contains one rotating jar in the fixed center position. The object has random three dimensional orientations and it has rotational symmetry with respect to the axis that connects the lid knob and the center point of the bottom. Therefore, the image is defined given the orientation of the lid knob. This indicates that the data has a  $S^2$  topology.

The cyclooctane dataset consists of 6,040 points in  $\mathbb{R}^{24}$ , corresponding to conformations of the cyclooctane molecule ( $C_8H_{16}$ ) Martin et al. (2010). A *conformation* is a configuration of atoms in a molecule up to rotation and translation of the molecule. Physical chemistry constraints for cyclooctane imply the positions of the 16 hydrogen atoms are determined by the positions of the 8 carbon atoms in each conformation Hendrickson (1967); Martin et al. (2010). Each point in the dataset consists of the 8 spatial coordinates of the carbon atoms flattened into a single vector, as in  $((x_1, y_1, z_1), (x_2, y_2, z_2), \ldots, (x_8, y_8, z_8))$  becomes  $(x_1, y_1, z_1, x_2, y_2, z_2, \ldots, x_8, y_8, z_8) \in \mathbb{R}^{24}$ .

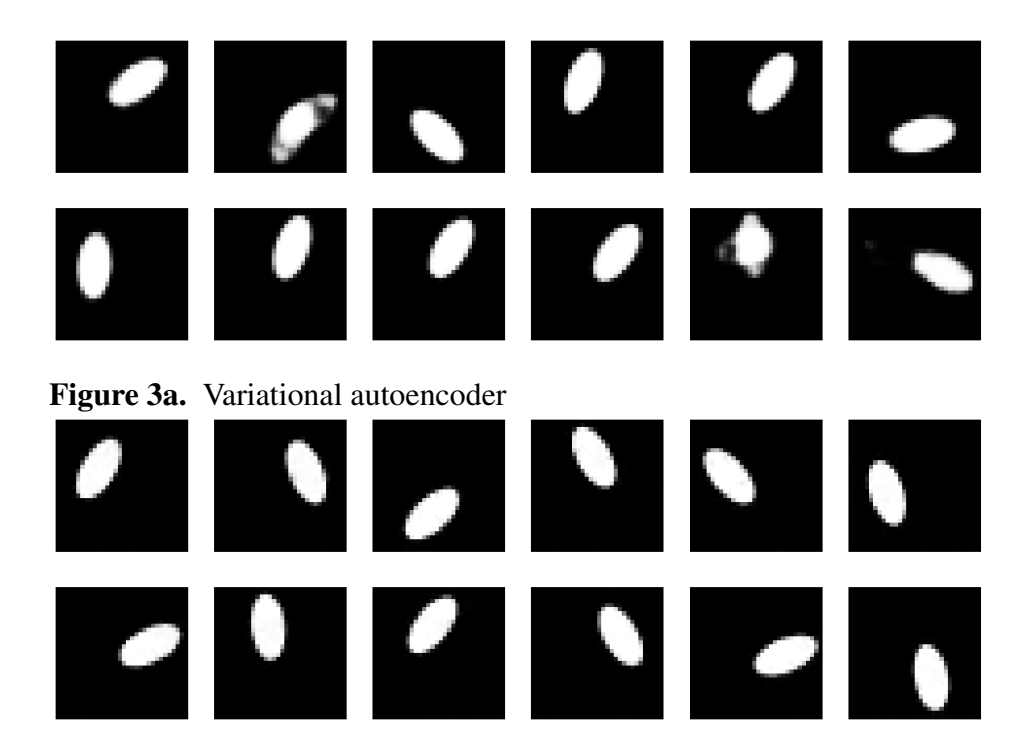


Figure 3b. Denoising diffusion probabilistic model

Figure 3. Random samples from different generators on "torus" ellipse image dataset.

# 3.2 Training setups

261

Here we introduce our training setups of different generative models. We adopted relatively simple 262 architectures that are capable of generating reasonably good quality samples. VAE and DDPM used for 263 the same dataset are designed to have a similar number of parameters, so that we know the performance 264 difference is not because of different parameter numbers. Training hyper-parameters, including learning 265 rates, epochs, weight values for VAE loss terms, and total time steps for DDPM, are determined using 266 Bayesian search (Falkner et al., 2018) over a set of different options. Therefore, the hyper-parameters for 267 268 each model are different but they are chosen to maximize the performance. Every model is trained using Adam optimizer (Kingma and Ba, 2015). For more details, see the supplementary materials. 269

# 270 3.3 Qualitative evaluation

- First, we evaluate each generative model qualitatively by observing randomly generated samples and interpolations between two data points.
- 273 Samples from generators trained on the "torus" dataset are shown in Figure 3. We can see that DDPM
- 274 produces high quality samples that are almost indistinguishable from ground truth images by human eyes.
- 275 The ellipses have clear edges and are always in the same correct shape. In contrast, VAE sometimes
- 276 generates clearly invalid images. The ellipse shapes are completely lost in some cases. Figure 5 shows
- 277 samples from DGM trained on the rotating jar. Both VAE and DDPM generally produce credible images.
- 278 However, we can see that VAE occasionally fails and generates misshapen jars. These results could be due
- 279 to VAE not learning the correct topology of the dataset and possibly sampling on the "holes" of the torus or
- 280 the sphere. We will explore this further in the following subsections.

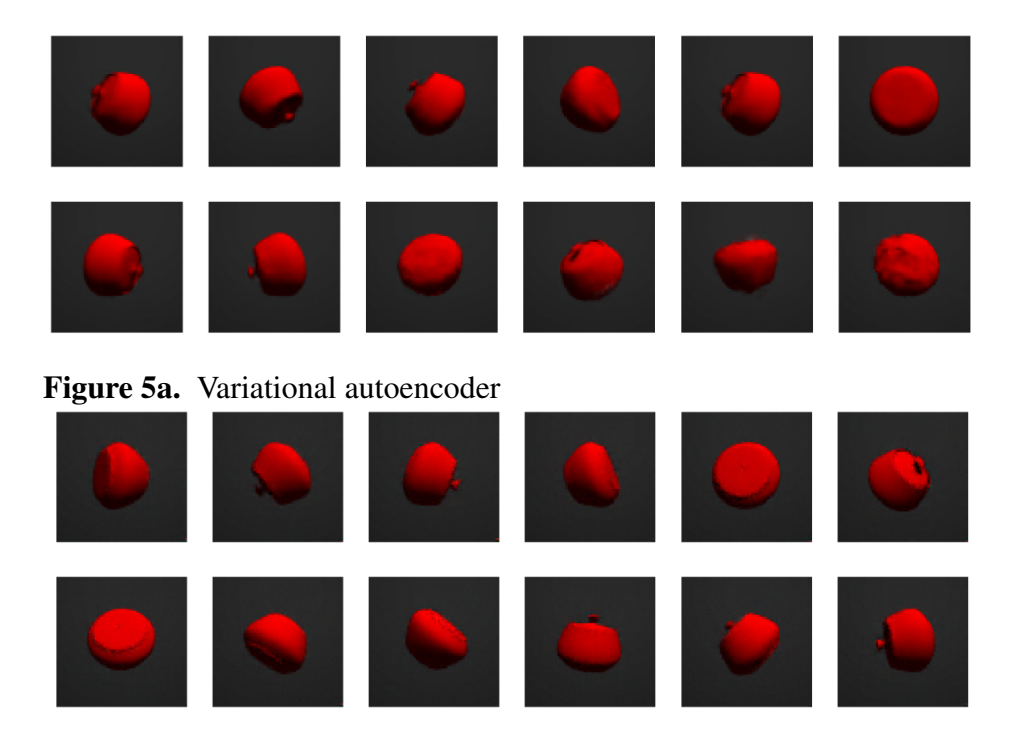


Figure 5b. Denoising diffusion probabilistic model

Figure 5. Random samples from different generators on rotating jar image dataset.

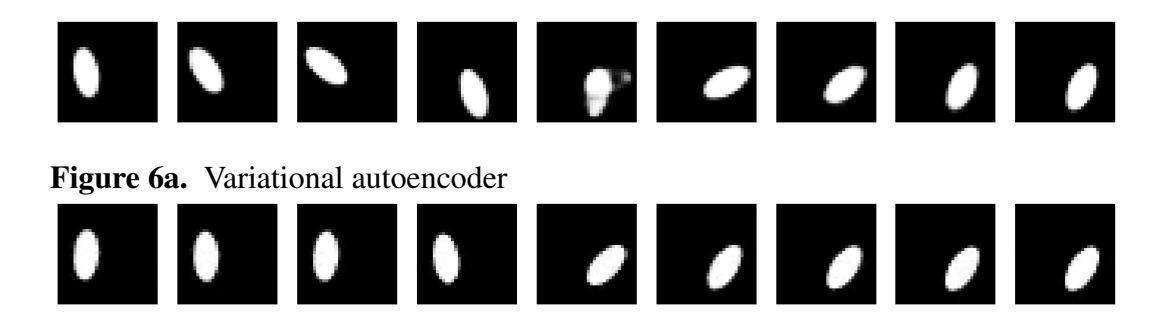


Figure 6b. Denoising diffusion probabilistic model

Figure 6. Interpolations from different generators on "torus" ellipse image dataset.

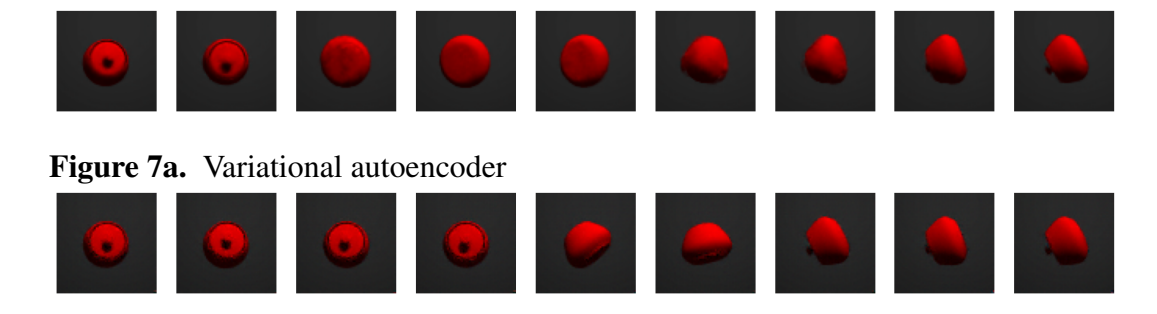
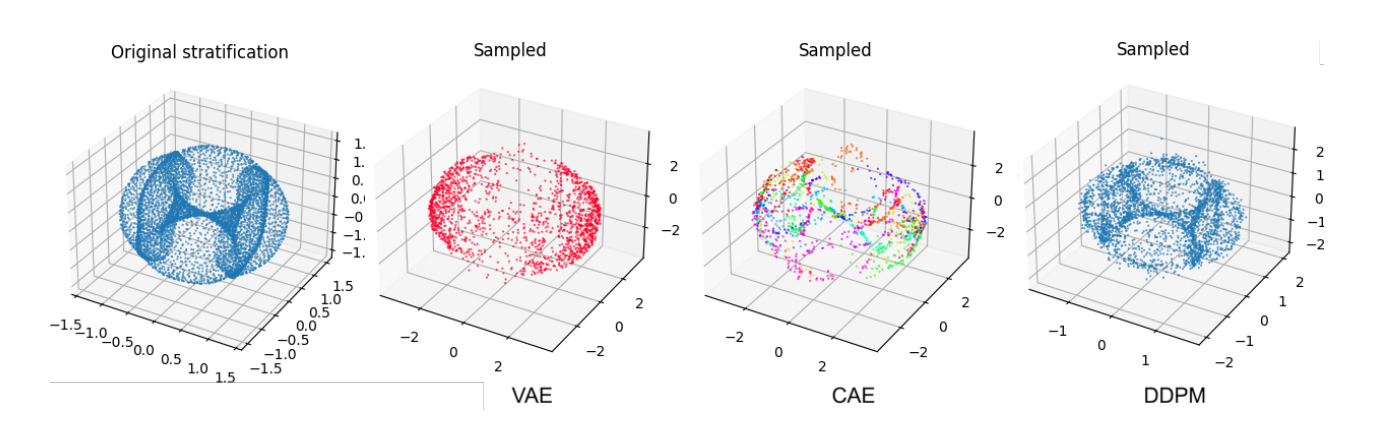


Figure 7b. Denoising diffusion probabilistic model

Figure 7. Interpolations from different generators on rotating jar image dataset.



**Figure 8.** A comparison of the cyclooctane conformations generated by sampling the various diffusion models. On the left, we display the Isomap embedding of the original cyclooctane data. For the CAE embeddings, the different colors denote the corresponding chart. Notice that the vanilla VAE struggles to generate the inner Klein bottle of the Isomap embedding. Counterintuitively, the DDPM generations most resemble the original data manifold even though its latent space is high dimensional.

We also performed interpolation between two data points using different generators, visualized in Figure 6 and 7. For the VAE, we linearly interpolate the latent space, which results in invalid images in the middle (5—th image for the "torus" and 3—rd image for the jar). We assume this happens because when we linearly interpolate between two points, we travel across the void of the latent distribution, where the VAE decoder cannot map to valid data points. For the DDPM, two end images are diffused for several time steps (t=250 for the "torus" and t=350 for the jar) and then linearly interpolated. Next, we apply the usual denoising steps until reversing back to t=0 to get clean images. Due to the stochasticity in both the forward and reverse processes, the endpoints will be different from the original images to a certain degree, depending on the diffusing time steps. We can also see that although the generated images look valid but do not provide a reasonably continuous interpolation. This can be considered as a shortcoming of DDPM not having a latent space.

In Figure 8, we see generated samples of cyclooctane under our different architectures. To visualize the conformations of cyclooctane, we embed the  $\mathbb{R}^{24}$  representations in  $\mathbb{R}^3$  using Isomap. This embedding is locally isometric and has been used in literature such as Martin et al. (2010). The original embedding of the dataset is visible on the left. Notice the geometry of this manifold involves a Klein bottle enveloped by a sphere. We find that the vanilla VAE struggles to generate conformations associated with the Klein bottle. This is not ideal as these conformations are associated with specific conformational states that do not correspond to any points on the outer sphere. Matching our intuition, the CAE is able to better cover the manifold of cyclooctane, where the embedded color represents chart membership. Still, we find the outer shell of the sphere is sparsely covered. Perhaps counterintuitively, the DDPM model visually best samples the data manifold. It is clear that the samples cover both the Klein bottle and the outer sphere with reasonable density.

# 3.4 Quantitative performance metrics

For each of the three datasets and each DGM, we computed the  $L_2$  Wasserstein metric between a sample set from the ground truth data distribution and a sample set generated by the DGM models. Because of the computational complexity of the Jonker-Volgenant algorithm, we were limited to computing with sample sizes of 3,000 data in both ground truth and DGM. To ensure that the metric values were stable at the given sample size, we repeated the metric calculation 10 times, each time with an independently

324

325 326

327

328 329

	"Torus" ellipse	Rotating jar	Cyclooctane
Ground truth VAE	$2.01 (\pm 0.15)$ $2.26 (\pm 0.05)$		$0.215 (\pm 0.009)$ $0.860 (\pm 0.004)$
DDPM CAE	$2.65\ (\pm 0.19)$		$0.389 (\pm 0.011)$ $0.860 (\pm 0.010)$

**Table 1.**  $L_2$  Wasserstein distance. Reporting mean and standard deviation over 10 independent runs, each time sampling n=3,000 images from both the ground truth data distribution and generators.

	"Torus" ellipse	Rotating jar	Cyclooctane
Ground truth & VAE	9.28e - 5	1.26e - 4	7.47e - 32
Ground truth & DDPM	1.30e - 7	4.04e - 17	8.70e - 19
Ground truth & CAE	-	-	2.04e - 29
VAE & DDPM	6.41e - 6	1.35e - 16	4.76e - 28
VAE & CAE	-	-	1
DDPM & CAE	-	-	3.50e - 26

**Table 2.** *p*-value of Wasserstein distance observations.

drawn sample from both the ground truth and the DGM. For the cyclooctane dataset, since we only have 309 6,040 samples in the ground truth data, we randomly draw 3,000 samples each time without replacement. 310 Results are shown in Table 1. Since the sample size used to approximate the Wasserstein distance is 311 312 limited, to rule out the effects of random sampling, we also performed t-tests on Wasserstein distance 313 observations and the resulting p-values are listed in Table 2. It is clear that the Wasserstein distances for different models are significantly different, except for between the VAE and CAE trained on cyclooctane, 314 which have very similar results. We can see that on the image datasets, VAE has a consistently smaller 315 distance to the ground truth data distribution than DDPM, despite what appears to be worse image quality 316 to human eyes. The result is different for the cyclooctane dataset, with DDPM having a significantly smaller 317 distance while CAE has a similar result to VAE. This should indicate in some datasets VAE is learning the 318 overall distribution better than DDPM. It could be the case that in terms of  $L_2$  distance, although DDPM 319 samples are more precise, or more close to the ground truth distribution, VAE samples cover the whole 320 data distribution better. And we can also see that the probability based metric alone does not sufficiently 321 represent the real world performance of models. 322

For the cyclooctane dataset, we calculated the bond lengths of generated samples and compared them to the bond lengths of the true cyclooctane data. Bond lengths for the true data are tightly distributed about the mean value of 1.52~Å with a standard deviation of  $4.09\text{e}{-5}~\text{Å}$ . Figure 9 shows the distribution of each sample set's bond lengths. We can see that although the sample bond lengths of all the generative models are much more dispersed than the ground truth values, DDPM has a relatively better distribution. The expected errors of each distribution to the mean ground truth value are also calculated. This error is 0.165~Å for VAE, 0.155~Å for CAE and 0.04~Å for DDPM.

	"Torus" ellipse	Rotating jar
VAE	16.77	77.72
DDPM	15.00	74.90

**Table 3.** Torchmetrics implementation of FID using 50,000 samples. Lower is better.

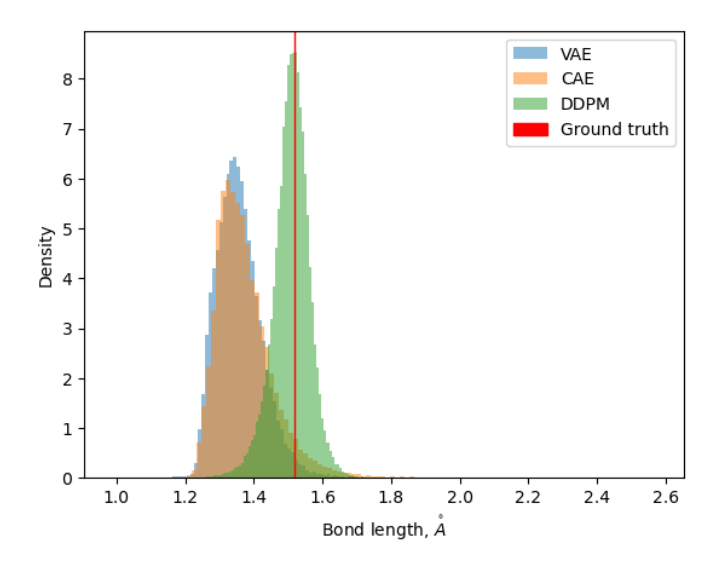


**Figure 9.** Density histogram of bond lengths of samples generated by different models, compared to the ground truth bond lengths.

	"Torus" ellipse	Rotating jar
VAE	0.895 / 0.878	0.403 / 0.605
DDPM	0.903 / 0.951	0.943 / 0.903

**Table 4.** Density / Coverage. Reference implementation from Naeem et al. (2020) with k=5 and torchvision pretrained VGG16 "IMAGENET1K\_V1" as the embedding. 50,000 samples. Density is positively valued, with a value of 1 being ideal; values greater than 1 represent generated data occurring near common modes in the real data more often, and values less than 1 represent generated data occurring less often near real data. Coverage is in the range [0, 1] with 1 being optimal; it represents the percentage of real points that are covered by a generated point.

We also computed deep-learning-based metrics - FID, density, and coverage, for our two image datasets. The sample sizes of 50,000 are used for both ground-truth data distribution and the DGM learned distribution. The deep learning model used for embedding is VGG16 "IMAGENET1K\_V1". The FID results are shown in Table 3, and density and coverage results are shown in Table 4. Unlike in the case of Wasserstein distance, DDPM constantly has better metrics values than VAE. This could indicate that the deep learning model used to embed images does capture image features in a way that matches better with human visual experiences. The much larger sample size might also influence the results.

# 3.5 Topological Properties

We also report the persistent homology of ground truth data and samples from generators. Giottotda (Tauzin et al., 2021) is used to obtain the results. As introduced in Section 2.2.4, the results show when a topological feature was born and died. Zero-dimensional features are connected components, one-dimensional features are loops, and two-dimensional features are voids (e.g., spheres). The further a point on the persistence diagram is from the diagonal line of "birth = death", the longer they persist across a range of scales, that is, distance thresholds determining when points are connected. These points that stand out beyond the diagonal are more likely to indicate a topological structure.

As we can see in Figure 10a, the "torus" dataset has two significant one-dimensional loops (approximately (2.5, 8) and (2.5, 13)) and one two-dimensional sphere (approximately (6, 8)) because of its torus topology.

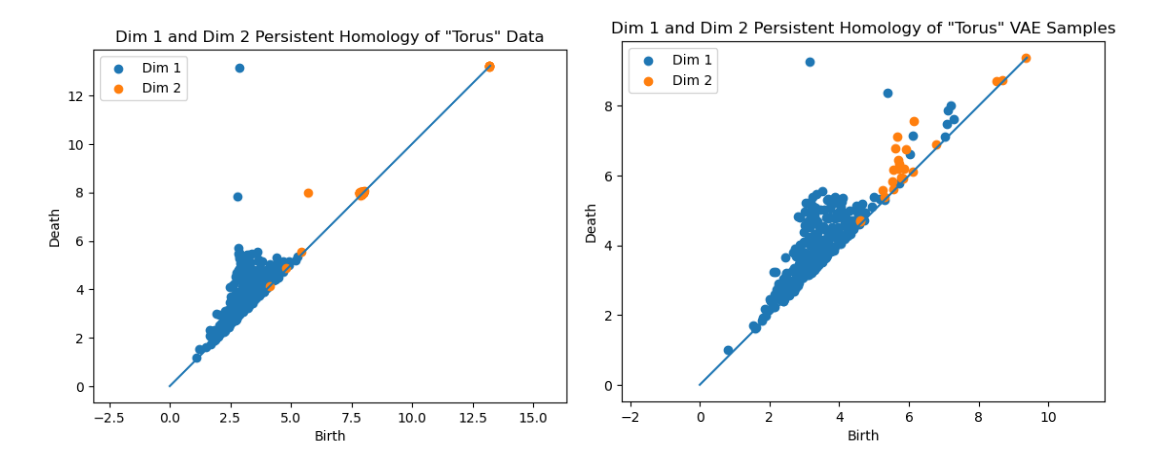


Figure 10a. Ground truth data

Figure 10b. Samples from VAE

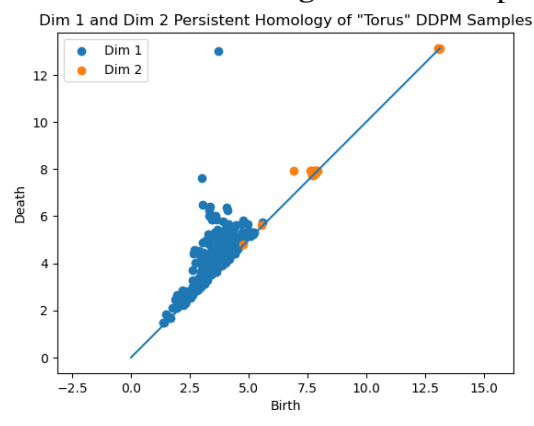


Figure 10c. Samples from DDPM

**Figure 10.** Persistent homology of ground truth data and generator samples on the "torus" dataset.

The VAE captures this topological structure poorly (Figure 10b), and only significantly captures one one-dimensional loop structure. Although there are many other points relatively far above the diagonal line, there are no points that stand out from the others clearly. On the other hand, DDPM preserves this structure very well (Figure 10c), and we can clearly identify two one-dimensional loops (the points located at approximately (3, 8) and (3.5, 13)) and one two-dimensional sphere (located at approximately (7, 8)).

This result gives insight into the fact that the VAE sometimes generates invalid samples despite its smaller Wasserstein distance. More intuitively, we show the PCA visualization of the data and the generator samples in Figure 11. We can clearly see that VAE wrongly generates samples in the middle of the torus and violates the original data topology, but DDPM does not. The results for the jar dataset are displayed in Figure 12. As we discussed above, the data has a spherical topology, which is indicated by a significant dimension 2 point in the persistence diagram in Figure 12a (located at approximately (5.5, 7.5)). This structure is clearly better preserved by DDPM (approximately (5.5, 7.5)). Whereas in the persistence diagram of the VAE model, the two-dimensional structure is much less significant, and also an incorrect one-dimensional loop appears (located at approximately (3, 5.5)).

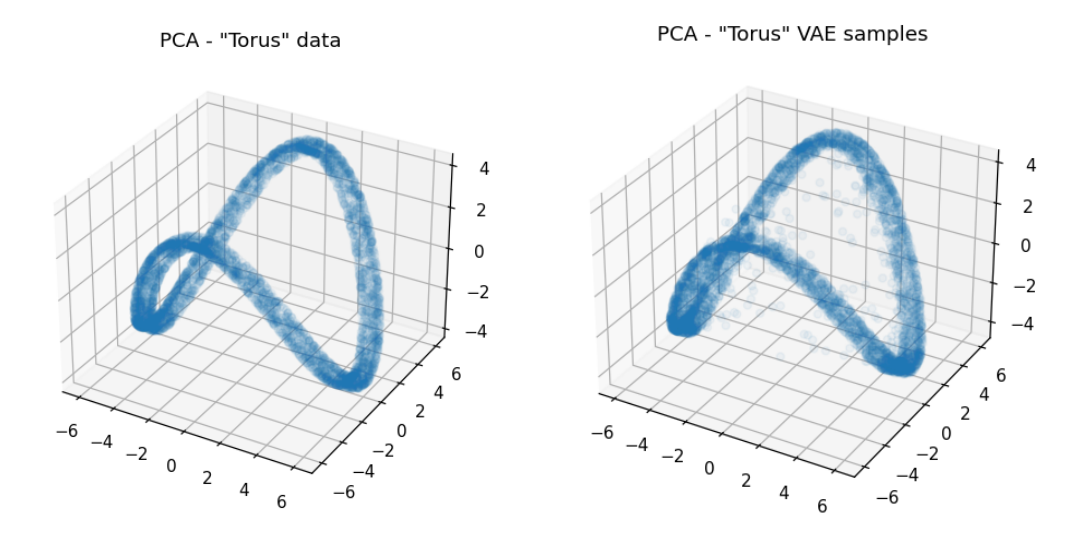
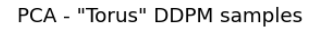


Figure 11a. Ground truth data

Figure 11b. Samples from VAE



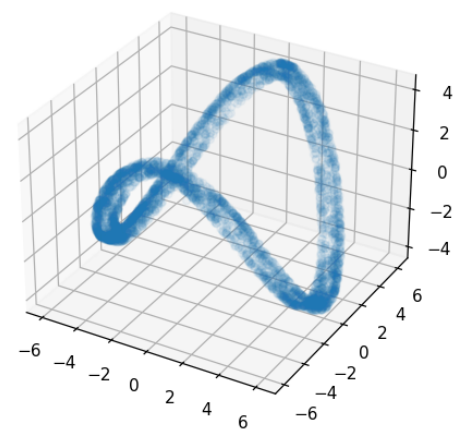


Figure 11c. Samples from DDPM

Figure 11. PCA visualizations of ground truth data and generator samples on the "torus" dataset.

# 4 DISCUSSION AND CONCLUSION

361

362

363

364

365

366

367

368

369

In this paper, we investigated the ability of DGMs to model data distributions with non-trivial topologies. We hypothesized that VAEs would struggle to faithfully model non-Euclidean topologies because they generate data by continuously transforming a Gaussian random vector from a lower-dimensional, Euclidean latent space. This hypothesis was supported by our experiments on datasets with known topology. Our results comparing persistence diagrams of generated VAE samples versus the ground truth persistence diagram show that a VAE does not faithfully recover the correct topology in the case of the torus ( $\mathbb{T}^2$ ) or the sphere ( $S^2$ ). We further hypothesize that a similar failure to capture topology would hold for other models based on a Euclidean latent space, e.g., GANs, although this would need to be verified with further experiments.

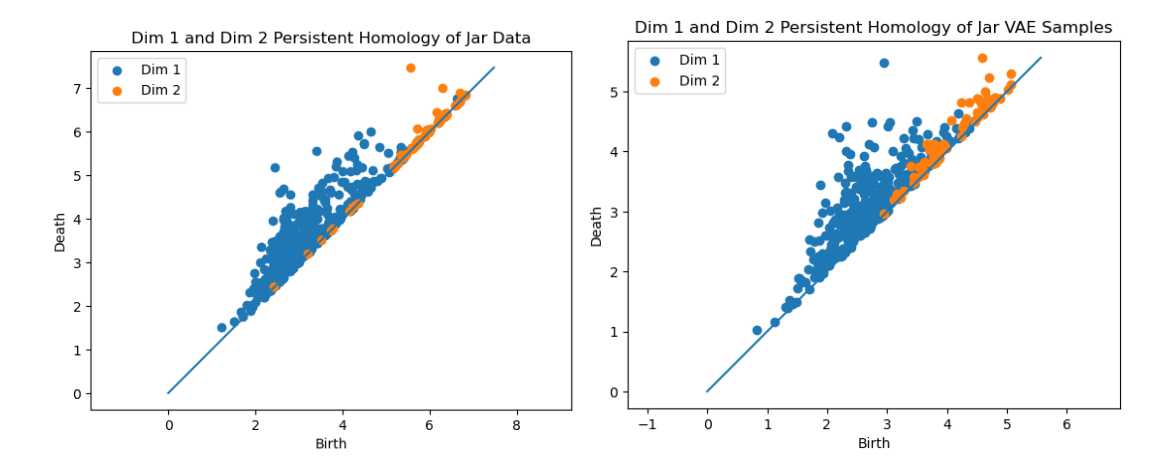


Figure 12a. Ground truth data

**Figure 12b.** Samples from VAE

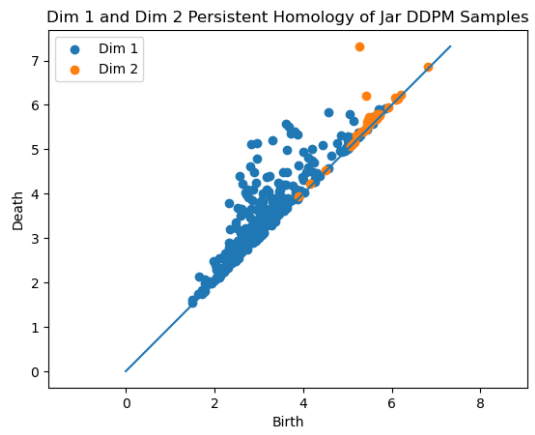


Figure 12c. Samples from DDPM

Figure 12. Persistent homology of the ground truth data and generator samples on jar dataset.

Conversely, we hypothesized that DDPM and related score-based models, which theoretically have no constraint on their topology and learn the distribution in the original data dimension, would more effectively capture non-trivial data topologies. This turned out to be the case in our image experiments, where the DDPM persistence diagrams showed that they generated samples with much better matches to the ground-truth data topology. Furthermore, the ability of DDPMs to adapt to the topology of the data may explain their improved performance in generating realistic data samples, as they can avoid sampling in "holes" of the data distribution. However, one downside to DDPMs is that they do not parameterize the data distribution with a low-dimensional latent space. This makes moving along the data manifold, such as in the case of interpolation, more difficult with DDPMs. The CAE model tries in a sense to bridge this gap by providing a low-dimensional latent space, while at the same time also providing more topological flexibility. Our cyclooctane results show qualitatively and quantitatively that the CAE performs well on a complex data topology.

One unexpected result is the disagreement between the  $L_2$  Wasserstein metric and the other quantitative metrics (FID, density, and coverage). It may be the case the restriction on the sample size for the Wasserstein metric limits its approximation accuracy. Or it may be the case that the exact matching of points between the two samples is prone to outliers or other artifacts in the samples. Or it may simply be that "perceptual distances" mimicked by the VGG16 network are substantially different enough from  $L_2$  distances to cause

- reverse conclusions in the two classes of metrics. This discrepancy, and the more general question of how to best measure the distribution quality of a DGM, are directions ripe for future research.
- In conclusion, our main novel contribution is the first test of the abilities of generative models to handle different data topologies. Our empirical findings highlight the limitations of a simplistic data topology assumption. The main takeaways are as follows:
- Generative models that assume data can be continuously mapped from a Euclidean latent space, e.g.,
  VAEs, have limited ability to capture more complex topologies present in data.
- Conversely, DDPMs operate in the full-dimensional data space and without assumptions about the data topology. This results in DDPMs being better able to capture non-trivial topologies in data.
- However, the absence of straightforward Euclidean latent spaces in DDPM presents obstacles,
  particularly in tasks such as interpolations.
- Finally, our research underscores that distribution-based evaluation metrics sometimes fail to provide a comprehensive assessment of a generative model's ability to accurately capture the underlying data topology.

# **CONFLICT OF INTEREST STATEMENT**

- 401 Author N.J.T. is employed by STR. The authors M.J.C., A.D.S., and P.B. are employed by Geometric Data
- 402 Analytics. The remaining authors declare that the research was conducted in the absence of any commercial
- 403 or financial relationships that could be construed as a potential conflict of interest.

#### **AUTHOR CONTRIBUTIONS**

- 404 Y.J. conducted experiments on image datasets and wrote part of the background and metrics section and
- 405 experiments section. R.M. calculated FID, density, and coverage values for image datasets and wrote the
- 406 introduction of these metrics and the corresponding results. N.J.T. and M.J.C conducted experiments on the
- 407 cyclooctane dataset and wrote the introduction of CAE and the results of cyclooctane experiments. A.D.S.,
- 408 P.B., M.B.D., and P.T.F. wrote the introduction, conclusion, part of the background and methods section,
- 409 and performed general editing.

#### **FUNDING**

- 410 This work was funded by Agreement HR0011-22-9-0076 from the Defense Advanced Research Projects
- 411 Agency (DARPA), as part of the Geometries of Learning (GoL) Artificial Intelligence Exploration (AIE)
- 412 program, by the National Science Foundation under awards 2019239 and 2129824, and by The Air Force
- 413 Office of Scientific Research under award number FA9550-21-0164.

# DATA AVAILABILITY STATEMENT

- 414 We have made available the Python code we developed for producing the ellipse images in the "torus"
- 415 dataset as a PyPI package here: https://pypi.org/project/ellipse/.

#### REFERENCES

- 416 Arvanitidis, G., Hansen, L. K., and Hauberg, S. (2018). Latent space oddity: On the curvature of deep
- generative models. In *Proceedings of the 6th International Conference on Learning Representations*,
- 418 *ICLR 2018*
- 419 Barannikov, S., Trofimov, I., Sotnikov, G., Trimbach, E., Korotin, A., Filippov, A., et al. (2021). Manifold
- 420 topology divergence: A framework for comparing data manifolds. In *Proceedings of Advances in Neural*
- 421 Information Processing Systems 34: Annual Conference on Neural Information Processing Systems
- 422 2021, NeurIPS 2021. 7294–7305
- 423 Borji, A. (2022). Pros and cons of GAN evaluation measures: New developments. Computer and Vision
- 424 *Image Understanding* 215, 103329
- 425 Carrière, M., Chazal, F., Ike, Y., Lacombe, T., Royer, M., and Umeda, Y. (2020). Perslay: A neural
- network layer for persistence diagrams and new graph topological signatures. In *Proceedings of the 23rd*
- 427 International Conference on Artificial Intelligence and Statistics, AISTATS 2020. vol. 108, 2786–2796
- 428 Chen, C., Ni, X., Bai, Q., and Wang, Y. (2019). A topological regularizer for classifiers via persistent
- 429 homology. In Proceedings of the 22nd International Conference on Artificial Intelligence and Statistics,
- 430 *AISTATS 2019*. vol. 89, 2573–2582
- 431 Chen, N., Klushyn, A., Kurle, R., Jiang, X., Bayer, J., and van der Smagt, P. (2018). Metrics for deep
- 432 generative models. In *Proceedings of the 21st International Conference on Artificial Intelligence and*
- 433 Statistics, AISTATS 2018. vol. 84, 1540–1550
- 434 Chong, M. J. and Forsyth, D. (2020). Effectively unbiased FID and Inception Score and where to find them.
- 435 *arXiv:1911.07023*
- 436 Cohen-Steiner, D., Edelsbrunner, H., and Harer, J. (2007). Stability of persistence diagrams. Discrete &
- 437 *Computational Geometry* 37, 103–120
- 438 Du, Y. and Mordatch, I. (2019). Implicit generation and generalization in energy-based models.
- 439 arXiv:1903.08689
- 440 Edelsbrunner, H. and Harer, J. (2010). Computational Topology an Introduction (American Mathematical
- 441 Society
- 442 Falkner, S., Klein, A., and Hutter, F. (2018). BOHB: robust and efficient hyperparameter optimization at
- scale. In Proceedings of the 35th International Conference on Machine Learning, ICML 2018. vol. 80,
- 444 1436–1445
- 445 Fasy, B. T., Lecci, F., Rinaldo, A., Wasserman, L., Balakrishnan, S., and Singh, A. (2014). Confidence sets
- for persistence diagrams. *Annals of Statistics* 42, 2301–2339
- 447 Genevay, A., Peyré, G., and Cuturi, M. (2018). Learning generative models with sinkhorn divergences. In
- 448 International Conference on Artificial Intelligence and Statistics, AISTATS 2018. vol. 84, 1608–1617
- 449 Goodfellow, I. J., Pouget-Abadie, J., Mirza, M., Xu, B., Warde-Farley, D., Ozair, S., et al. (2014).
- 450 Generative adversarial nets. In *Proceeding of Advances in Neural Information Processing Systems 27:*
- 451 Annual Conference on Neural Information Processing Systems 2014, NEURIPS 2014. 2672–2680
- 452 Hendrickson, J. B. (1967). Molecular geometry. V. Evaluation of functions and conformations of medium
- rings. *Journal of the American Chemical Society* 89, 7036–7043
- 454 Hensel, F., Moor, M., and Rieck, B. (2021). A survey of topological machine learning methods. Frontiers
- *in Artificial Intelligence* 4, 681108
- 456 Heusel, M., Ramsauer, H., Unterthiner, T., Nessler, B., and Hochreiter, S. (2017). GANs trained by a two
- 457 time-scale update rule converge to a local nash equilibrium. Advances in neural information processing
- 458 systems 30, 6626–6637

- 459 Hinton, G. E. and Salakhutdinov, R. R. (2006). Reducing the dimensionality of data with neural networks.
- 460 Science 313, 504–507
- 461 Ho, J., Jain, A., and Abbeel, P. (2020). Denoising diffusion probabilistic models. Advances in neural
- 462 information processing systems 33, 6840–6851
- 463 Jonker, R. and Volgenant, T. (1988). A shortest augmenting path algorithm for dense and sparse linear
- assignment problems. In *Proceedings of the 16th Annual Meeting of DGOR in Cooperation with NSOR*.
- 465 622–622
- 466 Khrulkov, V. and Oseledets, I. V. (2018). Geometry score: A method for comparing generative adversarial
- networks. In Proceedings of the 35th International Conference on Machine Learning, ICML 2018.
- 468 vol. 80, 2626–2634
- 469 Kingma, D. P. and Ba, J. (2015). Adam: A method for stochastic optimization. In 3rd International
- 470 Conference on Learning Representations, ICLR 2015
- 471 Kingma, D. P. and Welling, M. (2014). Auto-encoding variational Bayes. In Proceedings of the 2nd
- 472 International Conference on Learning Representations, ICLR 2014
- 473 Martin, S., Thompson, A., Coutsias, E. A., and Watson, J.-P. (2010). Topology of cyclo-octane energy
- landscape. The Journal of Chemical Physics 132, 234115
- Naeem, M. F., Oh, S. J., Uh, Y., Choi, Y., and Yoo, J. (2020). Reliable fidelity and diversity metrics for
- 476 generative models. In *Proceedings of the 37th International Conference on Machine Learning, ICML*
- 477 2020. vol. 119, 7176–7185
- 478 Naitzat, G., Zhitnikov, A., and Lim, L.-H. (2020). Topology of deep neural networks. The journal of
- 479 *Machine Learning Research* 21, 184:7503–184:7542
- 480 Nigmetov, A. and Morozov, D. (2022). Topological optimization with big steps. arXiv:2203.16748
- 481 Otter, N., Porter, M. A., Tillmann, U., Grindrod, P., and Harrington, H. A. (2017). A roadmap for the
- computation of persistent homology. *EPJ Data Science* 6, 1–38
- 483 Oudot, S. Y. (2017). Persistence Theory: From Quiver Representations to Data Analysis (American
- 484 Mathematical Society)
- 485 Parmar, G., Zhang, R., and Zhu, J.-Y. (2022). On aliased resizing and surprising subtleties in GAN
- 486 evaluation. *arXiv:2104.11222*
- 487 Persistence of Vision Pty. Ltd. (2004). Persistence of vision raytracer (version 3.6) [computer software]
- 488 http://www.povray.org/download/
- 489 Rezende, D. J. and Mohamed, S. (2015). Variational inference with normalizing flows. In *Proceedings of*
- 490 the 32nd International Conference on Machine Learning, ICML 2015. vol. 37, 1530–1538
- 491 Sajjadi, M. S. M., Bachem, O., Lucic, M., Bousquet, O., and Gelly, S. (2018). Assessing generative models
- via precision and recall. In *Proceedings of Advances in Neural Information Processing Systems 31:*
- 493 Annual Conference on Neural Information Processing Systems 2018, NeurIPS 2018. 5234–5243
- 494 Schonsheck, S., Chen, J., and Lai, R. (2019). Chart auto-encoders for manifold structured data.
- 495 arXiv:1912.10094
- 496 Shao, H., Kumar, A., and Fletcher, P. T. (2018). The Riemannian geometry of deep generative models. In
- 497 Proceedings of 2018 IEEE Conference on Computer Vision and Pattern Recognition Workshops, CVPR
- 498 *Workshops 2018.* 315–323
- 499 Shukla, A., Uppal, S., Bhagat, S., Anand, S., and Turaga, P. K. (2018). Geometry of deep generative
- models for disentangled representations. In Proceedings of ICVGIP 2018: 11th Indian Conference on
- 501 Computer Vision, Graphics and Image Processing. 68:1–68:8

- 502 Sohl-Dickstein, J., Weiss, E. A., Maheswaranathan, N., and Ganguli, S. (2015). Deep unsupervised learning using nonequilibrium thermodynamics. In *Proceedings of the 32nd International Conference*
- on Machine Learning, ICML 2015. vol. 37, 2256–2265
- 505 Solomon, E., Wagner, A., and Bendich, P. (2021). A fast and robust method for global topological
- functional optimization. In *Proceedings of the 24th International Conference on Artificial Intelligence* and Statistics, AISTATS 2021. vol. 130, 109–117
- 508 Song, Y., Sohl-Dickstein, J., Kingma, D. P., Kumar, A., Ermon, S., and Poole, B. (2021). Score-based
- 509 generative modeling through stochastic differential equations. In *Proceedings of the 9th International*
- 510 Conference on Learning Representations, ICLR 2021
- 511 Tauzin, G., Lupo, U., Tunstall, L., Pérez, J. B., Caorsi, M., Medina-Mardones, A. M., et al. (2021).
- 512 giotto-tda: : A topological data analysis toolkit for machine learning and data exploration. *Journal of*
- 513 *Machine Learning Research* 22, 39:1–39:6
- Virtanen, P., Gommers, R., Oliphant, T. E., Haberland, M., Reddy, T., Cournapeau, D., et al. (2020). SciPy
- 515 1.0: Fundamental Algorithms for Scientific Computing in Python. *Nature Methods* 17, 261–272
- 516 Wheeler, M., Bouza, J., and Bubenik, P. (2021). Activation landscapes as a topological summary of neural
- 517 network performance. In *Proceedings of 2021 IEEE International Conference on Big Data*. 3865–3870